SUPPLEMENTAL MATERIAL
Optically Probing Tunable Band Topology in Atomic Monolayers

Gaofeng Xu,[1] Tong Zhou,[1] Benedikt Scharf,[2] and Igor Žutić[1]

[1]*Department of Physics, University at Buffalo, State University of New York, Buffalo, NY 14260, USA*
[2]*Institute for Theoretical Physics and Astrophysics and Würzburg-Dresden Cluster of Excellence ct.qmat, University of Würzburg, Am Hubland, 97074 Würzburg, Germany*

(Dated: September 9, 2020)

I. ELECTRONIC STRUCTURE OF BISMUTHENE AND ANTIMONENE

As an emerging group of two-dimensional (2D) materials, bismuth and antimony thin films have been recently attracting increasing attention in the field of topological matter due to their strong spin-orbit coupling (SOC) and various topological states [1, 2]. Especially, bismuthene, fabricated on a SiC substrate [Fig. S1(a)] was experimentally found to be a 2D topological insulator with a record nontrivial band gap of 0.8 eV [3]. However, such a gap in bismuthene is indirect [see Fig. S1(b)] because of the huge SOC of Bi atoms, which is unlikely to support excitons. To get a direct gap, we turn to a system with a smaller SOC: antimonene on a SiC substrate (Sb/SiC). Unlike Bi/SiC, a direct gap of 248 meV [Fig. S1(c)] was obtained in Sb/SiC. Such a band structure, well described by the effective Hamiltonian H_0 in main text, supports a gapped chiral fermion (CF) system [4], which is a good platform to explore the band topology-related optical response. To get our proposed spin- and valley-dependent Hamiltonian H, the staggered potential and exchange field can be induced to antimonene by changing SiC to a magnetic substrate [5]. In addition to using a suitable substrate, hydrogen passivation is another method to realize a CF system with a direct nontrivial gap of 410 meV in a hydrogenated antimonene (SbH) [Fig. S1(d)], as shown in Fig. S1(f). With doping of transition metal (TM) atoms [6], we can also induce the staggered potential and exchange field into antimonene to get our desired Hamiltonian. Such Sb/SiC and SbH systems give a strong material support to our theoretical model.

In experiments, the W-doped monolayer (ML) SbH [Fig. 4(a)] proposed in this work can be realized in two steps based on ML SbH [Fig. S1(d)]. (1) Partially remove the H atoms on the top surface of SbH. There are two atomic layers of H atoms in SbH, where the H atoms on the top (bottom) surface bond with A (B) sublattice of Sb atoms, as shown in Fig. S1(d) [7]. Considering that 2D materials are usually supported by a substrate, we assume the bottom surface of SbH is facing with the substrate and the top surface is exposed. Using the common chemical surface decoration method [8] or scanning tunneling microscope [9], the H atoms on the top surface (A sublattice) of SbH can be partially removed, while the bottom surface is unlikely to be affected because of the substrate. (2) Deposit W atoms to the H-deficient SbH. Since the p_z orbitals of the Sb atoms without H atoms are unbonded, the W atoms favor to be adsorbed and bond with such unbonded $\mathrm{Sb_A}$ atoms, rather than going to the bonded $\mathrm{Sb_B}$ sublattice. To verify this, we performed the structure relaxations for the structures of 2×2 SbH supercells with one W atom doped in A and B sublattices on the top surface [Fig. 4(a)], respectively. It was found the structure of 2×2 SbH supercells with one W atom doped in A sublattice is stable during the structure relaxation, which is also confirmed by the calculation

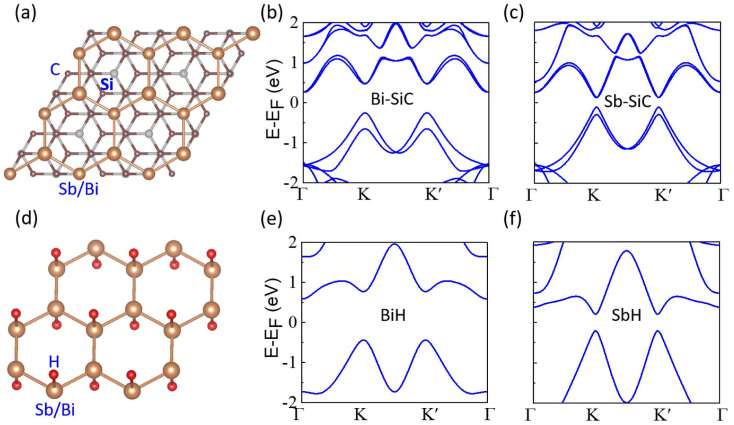

Fig. S 1: (a)-(c) Structure of planar antimonene/bismuthene on a SiC substrate and corresponding electronic structures. (d)-(f) Structure of hydrogenated planar antimonene (SbH)/bismuthene (BiH) and corresponding electronic structures.

of binding energies E_b, defined as $E_b = E_W + E_{Sb8H7} - E_{WSb8H7}$, where E_W, E_{Sb8H7}, and E_{WSb8H7} denote the total energies of the single W atom, 2×2 SbH supercells with one H atom removed, and 2×2 SbH supercells with one H atom in A sublattice substituted by a W atom [Fig. 4(a)], respectively. The obtained binding energy is 2.1 eV, comparable to that of most elemental crystalline solids [10]. However, for 2×2 SbH supercells with one W atom doped in the B sublattice, the structure is not stable during the structure relaxation. Thus, the W atoms favor to be adsorbed in A sublattice with H atoms removed. This surface-chemistry route has been widely used to create new materials with desirable features in [11, 12], suggesting experimental feasibility of fabricating the proposed W-doped ML SbH. The disorder of the W atoms has only a small influence on the low-energy properties of W-doped SbH (see Sec. XI), facilitating the experimental observation of the proposed effects.

II. GAPPED CHIRAL FERMION (CF) MODEL AND THE WINDING NUMBER

In this section, we provide a brief description of the gapped CF model and the associated winding number, as well as the optical selection rule proposed in Ref. [4]. The Hamiltonian for an isotropic 2D CF model is generally expressed as

$$H_{CF} = \begin{bmatrix} \Delta & \alpha(k)\exp(iw\phi_k) \\ \alpha(k)\exp(-iw\phi_k) & -\Delta \end{bmatrix}, \tag{II.1}$$

where w is the winding number, 2Δ is the gap, $\phi_k = \tan^{-1}(k_y/k_x)$ is the angle of $\mathbf{k}$, and $\alpha(k)$ is a function depending on specific material systems. Due to the rotational symmetry of the system, excitons can be labeled by the angular quantum numbers, m. The optical selection rule states that excitons with $m = w \pm 1$ are bright with respect to negative and positive helicities of light, respectively. Furthermore, to account for the crystal field effect in a crystal with N-fold rotational symmetry (C_N), bright excitons have angular quantum numbers $m = w \pm 1 \pmod N$, i.e., up to modulo N.

III. BETHE-SALPETER EQUATION

We have employed the procedure described in Refs. 13–15 to calculate neutral excitons. Since intervalley coupling is neglected, the excitons are calculated for each valley separately. We focus on neutral excitons with momentum $q_{\text{exc}} = 0$, which can be labeled by their quantum number S and valley index τ and calculated from the Bethe-Salpeter equation (BSE),

$$[\Omega_S^\tau - \epsilon_c^\tau(\mathbf{k}) + \epsilon_v^\tau(\mathbf{k})]\mathcal{A}_{vc\mathbf{k}}^{S\tau} = \sum_{v'c'\mathbf{k}'} \mathcal{K}_{vc\mathbf{k},v'c'\mathbf{k}'}^{\tau}\mathcal{A}_{v'c'\mathbf{k}'}^{S\tau}, \tag{III.1}$$

given as Eq. (9) in the main text [16]. Here, the band index $n = c(v)$ denotes one of the two conduction (valence) bands, $\epsilon_n^\tau(\mathbf{k})$ the corresponding single-particle/quasiparticle eigenenergies in valley τ with momentum $\mathbf{k}$, and Ω_S^τ the energy of the exciton state $|\Psi_S^\tau\rangle$. We have used the ansatz $|\Psi_S^\tau\rangle = \sum_{vc\mathbf{k}} \mathcal{A}_{vc\mathbf{k}}^{S\tau}\hat{c}_{\tau c\mathbf{k}}^\dagger \hat{c}_{\tau v\mathbf{k}}|\text{GS}\rangle$ for the exciton state with the coefficients $\mathcal{A}_{vc\mathbf{k}}^{S\tau}$, the creation (annihilation) operator of an electron in a conduction band c (valence band v) $\hat{c}_{\tau c\mathbf{k}}^\dagger$ ($\hat{c}_{\tau v\mathbf{k}}$) in valley τ, and the ground state $|\text{GS}\rangle$ with fully occupied valence bands and unoccupied conduction bands.

The BSE [Eq. (III.1)] describes an eigenvalue problem with an eigenvalue Ω_S^τ and an eigenvector $\mathcal{A}_{vc\mathbf{k}}^{S\tau}$. Since only intravalley Coulomb interactions are taken into account, the interaction kernel [13], consists of the direct and exchange terms,

$$\mathcal{K}_{vc\mathbf{k},v'c'\mathbf{k}'}^{\tau} = \mathcal{K}_{vc\mathbf{k},v'c'\mathbf{k}'}^{\text{d},\tau} + \mathcal{K}_{vc\mathbf{k},v'c'\mathbf{k}'}^{\text{x},\tau}, \tag{III.2}$$

$$\mathcal{K}_{vc\mathbf{k},v'c'\mathbf{k}'}^{\text{d},\tau} = -\int \mathrm{d}^2r\mathrm{d}^2r' W(\mathbf{r}-\mathbf{r}')\left\{[\psi_{c\mathbf{k}}^\tau(\mathbf{r})]^\dagger \psi_{c'\mathbf{k}'}^\tau(\mathbf{r})\right\}\left\{[\psi_{v'\mathbf{k}'}^\tau(\mathbf{r}')]^\dagger \psi_{v\mathbf{k}}^\tau(\mathbf{r}')\right\}, \tag{III.3}$$

$$\mathcal{K}_{vc\mathbf{k},v'c'\mathbf{k}'}^{\text{x},\tau} = \int \mathrm{d}^2r\mathrm{d}^2r' V(\mathbf{r}-\mathbf{r}')\left\{[\psi_{c\mathbf{k}}^\tau(\mathbf{r})]^\dagger \psi_{v\mathbf{k}}^\tau(\mathbf{r})\right\}\left\{[\psi_{v'\mathbf{k}'}^\tau(\mathbf{r}')]^\dagger \psi_{c'\mathbf{k}'}^\tau(\mathbf{r}')\right\}, \tag{III.4}$$

where $\psi_{n\mathbf{k}}^\tau(\mathbf{r})$ denote the wave functions of the single-particle states with energies $\epsilon_n^\tau(\mathbf{k})$ (see above), $V(\mathbf{r})$ the bare Coulomb potential determined from the dielectric environment, and $W(\mathbf{r})$ the screened Coulomb potential, all in real space.

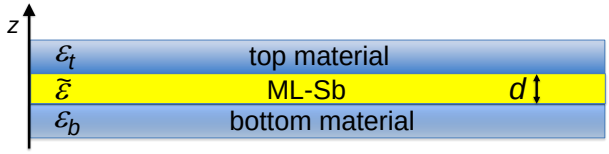

Fig. S 2: Geometry of the setup: a Sb-based monolayer of thickness d and dielectric constant $\tilde{\varepsilon}$ is embedded in two other materials with dielectric constants ε_t and ε_b.

The wave functions of the single-particle states $\psi^\tau_{n\mathbf{k}}(\mathbf{r}) = \exp(\mathrm{i}\mathbf{k}\cdot\mathbf{r})\eta^\tau_{n\mathbf{k}}/\sqrt{A}$ (with unit area A) are calculated from $H_\tau \eta^\tau_{n\mathbf{k}} = \epsilon^\tau_n(\mathbf{k})\eta^\tau_{n\mathbf{k}}$, with the single-particle Hamiltonian, $H_\tau = H_0 + H_{ex} + H_U + H_R$, defined in the main text. A substitution of $\psi^\tau_{n\mathbf{k}}(\mathbf{r})$ into Eqs. (III.3) and (III.4) leads to

$$\mathcal{K}^{\mathrm{d},\tau}_{vc\mathbf{k},v'c'\mathbf{k}'} = -\frac{W(\mathbf{k}-\mathbf{k}')\, f_{cc'}(\mathbf{k},\mathbf{k}')\, f_{v'v}(\mathbf{k}',\mathbf{k})}{A}, \tag{III.5}$$

$$\mathcal{K}^{\mathrm{x},\tau}_{vc\mathbf{k},v'c'\mathbf{k}'} = -\frac{V(\mathbf{k}-\mathbf{k}')\, f_{cv}(\mathbf{k},\mathbf{k})\, f_{v'c'}(\mathbf{k}',\mathbf{k}')}{A}, \tag{III.6}$$

where the form factors $f^\tau_{nn'}(\mathbf{k},\mathbf{k}') = [\eta^\tau_{n\mathbf{k}}]^\dagger \eta^\tau_{n'\mathbf{k}'}$ are calculated from the single-particle states, while $W(\mathbf{k})$ and $V(\mathbf{k})$ are the Fourier transforms of $W(\mathbf{r})$ and $V(\mathbf{r})$, defined below Eq. (III.4). Due to the orthogonality of the eigenspinors $\eta^\tau_{n\mathbf{k}}$, $f^\tau_{cv}(\mathbf{k},\mathbf{k}) = 0$, therefore $\mathcal{K}^{\mathrm{x},\tau}_{vc\mathbf{k},v'c'\mathbf{k}'}$ vanishes. Hence, the interaction kernel takes the form $\mathcal{K}^\tau_{vc\mathbf{k},v'c'\mathbf{k}'} = \mathcal{K}^{\mathrm{d},\tau}_{vc\mathbf{k},v'c'\mathbf{k}'}$ in our model. Moreover, $W(\mathbf{k})$ is needed to compute $\mathcal{K}^\tau_{vc\mathbf{k},v'c'\mathbf{k}'}$, which will be addressed in Sec. IV.

IV. COULOMB POTENTIAL AND GEOMETRIC CORRECTIONS

The bare Coulomb potential is determined by the dielectric environment and can be obtained from the Poisson equation. For the situation where the conduction bands are completely empty and all valence bands are occupied, the screened potential and the bare Coulomb potential, i.e., the potential unscreened by free charge carriers, coincide, $W(\mathbf{q}) = V(\mathbf{q})$. We consider the geometry shown in Fig. S2, for which the bare Coulomb potential between two electrons in the xy-plane of the intermediate layer ($z = z' = 0$) can be calculated as [17, 18]

$$V(\mathbf{q}) = \frac{2\pi e^2}{q} \frac{(\tilde{\varepsilon}^2 - \varepsilon_t\varepsilon_b) + (\tilde{\varepsilon}^2 + \varepsilon_t\varepsilon_b)\cosh(qd) + \tilde{\varepsilon}(\varepsilon_t + \varepsilon_b)\sinh(qd)}{\tilde{\varepsilon}\left[(\tilde{\varepsilon}^2 + \varepsilon_t\varepsilon_b)\sinh(qd) + \tilde{\varepsilon}(\varepsilon_t + \varepsilon_b)\cosh(qd)\right]}. \tag{IV.1}$$

For thin layers $qd \ll 1$, therefore $V(\mathbf{q})$ can be expanded in powers of qd, which yields

$$V(\mathbf{q}) \approx \frac{2\pi e^2}{\varepsilon q + r_0 q^2}, \tag{IV.2}$$

where $\varepsilon = (\varepsilon_t + \varepsilon_b)/2$ is the average dielectric constant of the bottom and top materials encapsulating the Sb-based monolayer (ML), and

$$r_0 = \frac{\tilde{\varepsilon} d}{2}\left(1 - \frac{\varepsilon_t^2 + \varepsilon_b^2}{2\tilde{\varepsilon}^2}\right), \tag{IV.3}$$

can be interpreted as the ML polarizability. In the limit of $\varepsilon_{t/b} \ll \tilde{\varepsilon}$, $r_0 = \tilde{\varepsilon} d/2$, we recover the result derived in Refs. 19, 20. The potential given by Eqs. (IV.2)-(IV.3) has proven to be successful in capturing the excitonic properties of ML-transition-metal dichalcogenides [21] and is used in our calculations. For W-doped ML SbH encapsulated by h-BN, the dielectric constants of the ML $\tilde{\varepsilon} = 10$ and encapsulating h-BN $\varepsilon_{t/b} = 3.8$.

V. GAUGE CHOICE

A specific gauge need to be chosen to calculate the velocity matrix elements, due to the phase arbitraryness in the eigenstates of the effective Hamiltonian [4, 22]. We fix the gauge by setting one component of the eigenstates real.

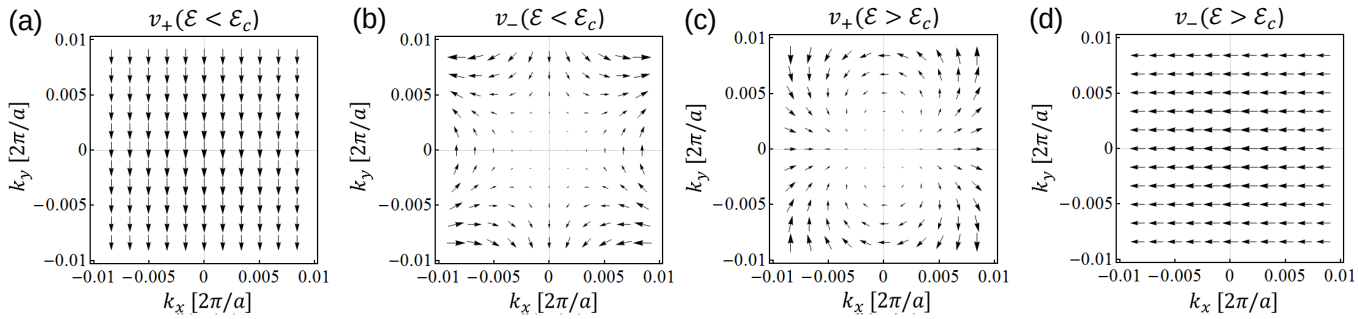

Fig. S 3: Full winding patterns of the interband matrix elements of the velocity operators $v_\pm(\mathbf{k})$ at the K' valley with the K' point at the origin. The real (imaginary) part of $v_\pm(\mathbf{k})$ is given along the horizontal (vertical) direction. (a) $v_+(\mathbf{k})$ and (b) $v_-(\mathbf{k})$ for $\mathcal{E} < \mathcal{E}_c$. (c) $v_+(\mathbf{k})$ and (d) $v_-(\mathbf{k})$ for $\mathcal{E} > \mathcal{E}_c$.

Specifically, we set the eigenstates of the Hamiltonian as

$$|c\mathbf{k}\rangle = \frac{|c_3|}{c_3}\begin{bmatrix} c_1 \\ c_2 \\ c_3 \\ c_4 \end{bmatrix}, \quad |v\mathbf{k}\rangle = \frac{|v_1|}{v_1}\begin{bmatrix} v_1 \\ v_2 \\ v_3 \\ v_4 \end{bmatrix}, \tag{V.1}$$

where c_i and v_i $(i = 1, 2, 3, 4)$ represent the complex components of the eigenvectors.

VI. DETAILS OF WINDING PATTERNS

In this section, we provide detailed discussions on the winding patterns mentioned in the main text. The full winding patterns of the interband matrix elements of the velocity operators $v_\pm(\mathbf{k})$ are given by Fig. S3, as a complement of Figs. 3 (a)-(d) in the main text, in which only one quarter ($k_x > 0$, $k_y > 0$) of each winding pattern is presented. The real and imaginary parts of each complex matrix element $v_\pm(\mathbf{k})$ are given by the horizontal and vertical lengths of a vector at $\mathbf{k}$. Therefore, the phases of velocity matrix elements are represented by the angles of the corresponding vectors.

As shown in Fig. S3, when $\mathcal{E} < \mathcal{E}_c$, the phase of $v_+(\mathbf{k})$ is nearly uniform, while $v_-(\mathbf{k})$ winds clockwise twice over a closed counterclockwise contour enclosing the K' point. In contrast, when $\mathcal{E} > \mathcal{E}_c$, $v_+(\mathbf{k})$ winds counterclockwise twice, while $v_+(\mathbf{k})$ is nearly uniform. Such a qualitative change of winding patterns reflects a change of the winding number of the bands. In a two-band model given by Eq. (II.1), the velocity matrix element has an angular dependence $v_\pm(\mathbf{k}) \propto \exp(-i(w \mp 1)\phi_{\mathbf{k}})$. Hence, this change of winding patterns is consistent with the change of winding number from 1 to -1, as given by the downfolded Hamiltonian Eqs. (4) and (5) in the main text. In addition, for a system with a rotational symmetry, an exciton envelop function can be expressed as a product of a radial and an angular part as $\mathcal{A}_{vc\mathbf{k}} = f_m(|\mathbf{k}|)e^{im\phi_{\mathbf{k}}}$. The corresponding oscillator strength of an optical transition to an exciton state with an angular quantum number m can be expressed as,

$$O_\pm^m \propto \left|\sum_{\mathbf{k}} f_m(|\mathbf{k}|)e^{im\phi_{\mathbf{k}}} v_\pm(\mathbf{k})\right|^2. \tag{VI.1}$$

To have a nonzero oscillator strength and thus significant optical transition, the angular part of the exciton envelop function has to be canceled by the angular dependence of the velocity matrix element $v_\pm(\mathbf{k})$, which are visualized by the winding of patterns. As we can see from the winding patterns in Fig. S3, nonzero oscillator strength for bright s excitons ($m = 0$) is achieved under σ^+ light when $\mathcal{E} < \mathcal{E}_c$; on the other hand, when $\mathcal{E} > \mathcal{E}_c$, s excitons are bright under σ^- light.

Note that in Ref. [22], winding patterns of monolayer, bilayer and trilayer gapped graphene systems have been calculated, showing changes of winding numbers for different layers of graphenes. However, in our proposal, the change of winding number is achieved in the same material by applying an external electric field. In addition, due to the time-reversal symmetry (TRS) in the systems considered in Refs. [4, 22] (MoS_2 and gapped graphene systems), the velocity matrix elements and their winding patterns at the K and K' valleys are related by the TRS. The absorption of one helicity of light in one valley is always accompanied by the absorption of the opposite helicity of light in the

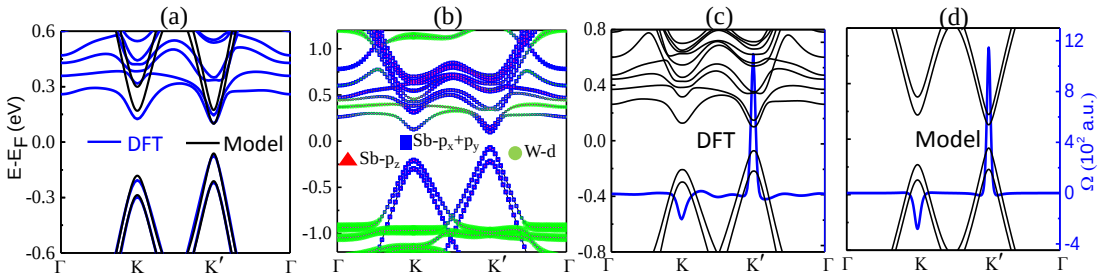

Fig. S 4: (a) The fitted bands of the effective model (black) for the DFT-calculated bands (blue) of W-doped 2×2 SbH supercells (W-2×2 SbH) without gating [Fig. 4(b) of the main text]. The obtained parameters are: $\lambda_{SO} = 0.19$ eV, $\lambda_R = 0.01$ eV, $M_A = 0.1$ eV, $M_B = 0.002$ eV, $U_i = 0.014$ eV, where U_i is the intrinsic staggered potential without gating. (b) The orbital-resolved electronic structure for (a). (c) and (d) Berry curvatures, Ω, for the whole valence bands of the W-2×2 SbH MLs calculated from DFT and effective model, respectively.

other valley, i.e., there is no net circular dichroism. However, TRS is broken by the exchange field in our system and therefore velocity matrix elements in the K and K' valleys are asymmetric, leading to a net circular dichroism. Hence, we have shown that the optical properties (circular dichroism) of a Sb-based monolayer can be tuned by an external electric field, which is of fundamental interest and can have potential application in atomically-thin optical electronic devices.

VII. COMPUTATIONAL DETAILS

To numerically solve Eq. (III.1) [Eq. (9) in the main text], a coarse uniform $N \times N$ k-grid with a spacing of $\Delta k = 2\pi/(Na_0)$ and $a_0 = 5.29$ Å in each direction is used. We also limit our calculation at an upper cutoff energy $E_{\rm cut}$. The value of Coulomb potential $W(\mathbf{k}-\mathbf{k}')$ at a coarse grid point $\mathbf{k}-\mathbf{k}'$ is obtained by averaging over a square centered at this grid point with sides Δk on a $N_{\rm int} \times N_{\rm int}$ fine grid, which has a spacing of $\Delta k_{\rm int} = \Delta k/N_{\rm int}$. For a proper convergence in our numerical calculations, we have used $N = 200$, $N_{\rm int} = 100$ and an energy cutoff of 600 meV above the band gap, i.e., $E_{\rm cut} = E_{\rm g}/2 + 600$ meV. We find that the $1s$ binding energy changes by less than 1% when going from $N = 200$ to $N = 300$. Parameters used in the calculations are: $\lambda_{SO} = 0.2$ eV, $\lambda_R = 0.02$ eV, $M_A = 0.1$ eV, $M_B = 0.002$ eV, $v_F = 8 \times 10^5$ m/s, $U_1 = 0.01$ eV, $U_2 = 0.08$ eV, which are based on literature [7] and our density functional theory (DFT) calculations, as shown in Fig. S4(a). To further show that the W atoms doped SbH monolayers (ML W-SbH) can be well described by our effective model based on p_x and p_y orbitals, we plot the orbital-resolved bands in Fig. S4 (b). It is clear that the bands near E_F are dominated by the Sb-p_x and Sb-p_y orbitals, while the bands from W atoms bonding with Sb-p_z orbitals are far away from E_F at the two valleys. Furthermore, the agreement between the Berry curvatures calculated from DFT [Fig. S4(c)] and the effective model [Fig. S4(d)] also provides additional support that the electronic structure and topological properties of ML W-SbH can be well described by our effective model.

The electronic ground-state calculations in this work were performed using the full-potential linearized augmented plane-wave (LAPW) method [23] as implemented in the WIEN2K code [24]. Spin-orbital coupling is included as a second vibrational step using scalar-relativistic eigenfunctions as the basis after the initial calculation is converged to self-consistency. The Perdew-Burke-Ernzerhof generalized-gradient approximation (PBE-GGA) [25] is used to describe the exchange and correlation functional. A vacuum space larger than 15 Å is set to avoid the interaction between the two adjacent layers. A Monkhorst-Pack k-grid of $9 \times 9 \times 1$ is adopted for the first Brillouin zone integral and the convergence criterion for the charge is 0.0001 e. To achieve a fully relaxed structure, all the atoms are allowed to move until the Hellmann-Feynman force on each atom is smaller than 0.01 eV/Å. The Berry curvature $\Omega(\mathbf{k})$ from all the valence bands is calculated by [6, 26]

$$\begin{aligned} \Omega(\mathbf{k}) &= \sum_n f_n \Omega_n(\mathbf{k}) \\ \Omega_n(\mathbf{k}) &= -2\,\mathrm{Im} \sum_{m \neq n} \frac{\langle \psi_{n\mathbf{k}} | v_x | \psi_{m\mathbf{k}} \rangle \langle \psi_{m\mathbf{k}} | v_y | \psi_{n\mathbf{k}} \rangle \hbar^2}{(E_m - E_n)^2}, \end{aligned} \tag{VII.1}$$

where E_n is the eigenvalue of the Bloch functions $|\psi_{n\mathbf{k}}\rangle$, f_n is the Fermi-Dirac distribution function at zero temperature, and v_x and v_y are the velocity operators.

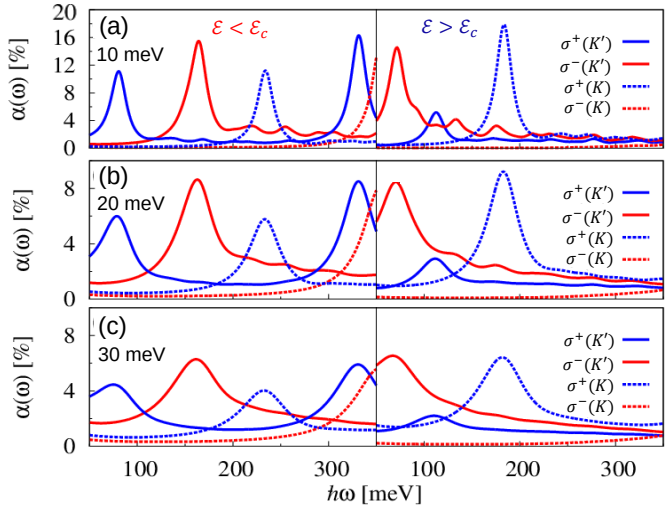

Fig. S 5: Absorption spectra for different broadenings from 10 to 30 meV. The other parameters are taken from Figs. 2(c) and (d).

VIII. EFFECT OF BROADENING

Broadening of the absorption spectra can be affected by various factors. For instance, broadening is strongly dependent on temperature and can increase by orders of magnitude from cryogenic to room temperatures. In our calculations, we chose a broadening of 20 meV to describe a room-temperature situation. To show the effect of broadening, in Fig. S5 we present calculated absorption spectra with broadening in a range from 10 to 30 meV.

From the series of spectra, we see that the qualitative feature of helicity reversal is not affected; only the widths of the peaks are directly modified along with the values of broadenings. This can be understood because broadening does not change the optical selection rules of excitons, which are determined by the corresponding winding numbers. We recall that Eq. (8) in the main text factorizes in a part $\left|\sum_{vc\mathbf{k}} v_{\pm}(\mathbf{k})\mathcal{A}^{S\tau}_{vc\mathbf{k}}\right|^2$ containing information about the selection rules and a part with the Lorentzian distribution $\delta(\hbar\omega - \Omega^{\tau}_S) = \Gamma/\left[\pi[(\hbar\omega - \Omega^{\tau}_S)^2 + \Gamma^2]\right]$ containing the broadening. Therefore, the helicities of the absorption peaks are not affected by a change of broadening.

IX. THE ANOMALOUS VALLEY HALL EFFECT: TRANSPORT RESPONSE TO THE TUNABLE BAND TOPOLOGY

In this section, we provide additional details and discussion about the transport response to the tunable band topology. Since in our system both inversion symmetry (IS) and TRS are broken, the valley splitting and nonzero Berry curvatures $\Omega(\mathbf{k})$ emerge in the valleys (Fig. 4 and Fig. S4), allowing us to identify signatures of a tunable band topology using transport detection beyond optical probes. As shown in Fig. S4(a), due to the exchange field induced valley splitting, a smaller gap and thus a lower energy of the $1s$ exciton appear in the K' valley compared to the K valley. Based on the gate-controlled tunability of the light helicity (Fig. 2), we know when $\mathcal{E} < \mathcal{E}_c$, σ^+ light with a frequency near resonance to the $1s$ exciton of the K' valley leads to significant excitation of carriers in the K' valley, but not in the K valley where it is off resonance. Thus the carrier density in K' valley ($n_{K'}$) is much larger than that in the K valley (n_K), giving a large carrier density imbalance (n_v) between the two valleys ($n_v = n_{K'} - n_K$). Due to the nonzero $\Omega(\mathbf{k})$ in the valleys [Fig. S4(c)], the photoexcited carriers in the K' valley experience a Lorentz-like force transverse to an in-plane electric field, $\mathcal{E}_{in}$, giving an anomalous valley Hall effect (AVHE) [27], described by an intrinsic anomalous Hall conductivity σ^+_H, as shown in Fig. S6(b). In contrast, when $\mathcal{E} > \mathcal{E}_c$, due to the change of the winding number and thus the helicity selectivity, the optical excitation and AVHE with σ^-_H is now only significant with σ^- light, as shown in Figs. S6(d)-(f). Theoretically, the helicity-dependent anomalous Hall conductivities σ^+_H and σ^-_H can be calculated from the integration of $\Omega(\mathbf{k})$ [$\sigma_H = (e^2/h)(1/2\pi)\int d^2k\Omega(\mathbf{k})$] [26] with $\mathcal{E} < \mathcal{E}_c$ and $\mathcal{E} > \mathcal{E}_c$, respectively. In the degenerate limit, σ_H can be approximated as $\sigma_H \sim n_v/E_g$ [27], where E_g is the band gap. Since n_v corresponds directly to the light helicity (band topology), the band topology can be probed by the detection of σ_H for each helicity of light separately, where a significant contrast in the Hall conductance is

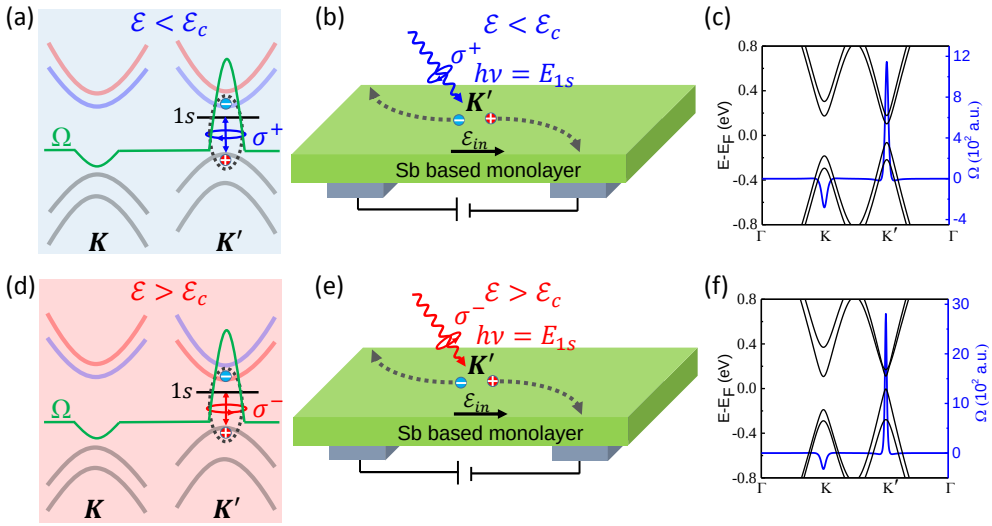

Fig. S 6: Distinguishing tunable band topology for $\mathcal{E} < \mathcal{E}_c$ and $\mathcal{E} > \mathcal{E}_c$ through transport response from an anomalous valley Hall effect (AVHE). (a) Schematic resonant optical excitation of $1s$ excitons with σ^+ light and nonzero Berry curvature Ω at the K/K' valleys, (b) the corresponding AVHE when an in-plane electric field, $\mathcal{E}_{in}$, is applied, and (c) calculated Ω from the effective model, all for $\mathcal{E} < \mathcal{E}_c$. An analogous situation for (d) excitation of $1s$ excitons with σ^- light, (e) AVHE, and (f) calculated Ω, all for $\mathcal{E} > \mathcal{E}_c$.

expected. Specifically, when $\mathcal{E} < \mathcal{E}_c$, $\sigma_H^+/\sigma_H^- \gg 1$; while $\mathcal{E} > \mathcal{E}_c$, $\sigma_H^+/\sigma_H^- \ll 1$. Therefore, an electrical detection of the band topology and winding number can be achieved. Furthermore, the asymmetry of gaps in the K/K' valleys leads to different energies of $1s$ excitons in the two valleys. Therefore, circularly polarized light as depicted in Fig. S6 is not necessary, valley polarization and AVHE can instead be achieved with linearly polarized light with a proper frequency. In MoS_2 systems, TRS has to be explicitly broken by shining circularly polarized light in order to create a population imbalance between the two valleys and observe VHE [27]. However, in our system, since valley splitting is achieved by the exchange field, a linearly polarized light with a suitable frequency can already lead to a valley polarization and the observation of AVHE. Such a transport response provides another approach to probe the gate-controlled band topology.

X. THE MECHANISM OF THE BAND-TOPOLOGY TUNABILITY

Here we illustrate the mechanism of the band-topology tunability in the antimonene system. Generally, there are three requirements in our proposal: (1) Directly gapped chiral fermions in the valleys, (2) exchange field ($\bar{M}$) to break TRS and thus to induce valley splitting, (3) staggered potential (U) to break IS, which is also controllable by an electric field. In our proposed example of W-doped ML SbH, all three of the above requirements are fulfilled. For (1) pristine ML SbH has a direct gap with chiral fermions as shown in Fig. S1, while for (2) and (3) the W atoms induce both the exchange field and staggered potential.

To illustrate how $\bar{M}$ and U are induced in ML SbH by W-atoms and tuned by the electric field, we plot the bands of the pristine ML SbH and W-2×2 SbH without SOC, in Fig. S7(a) and (b), respectively. Since both the IS and TRS are preserved in ML SbH, degenerate Dirac cones exist at the valleys, as shown in Fig. S7(a). When one H atom at the Sb_A sublattice is replaced by a W atom [shown in Fig. 4(a)], a calculated magnetic moment of $\sim 5\mu_B$ is induced in the system, breaking TRS and thus resulting in spin-polarized bands as shown in Fig. S7(b). The W atoms also break the inversion symmetry of ML SbH, inducing an intrinsic staggered potential, U_i, between the Sb_A and Sb_B sublattices, giving rise to different gaps between conduction and valence bands for spin-up and spin-down levels, respectively, shown in Fig. S7(b).

From a tight-binding model constructed as in our previous work [5, 28], both $\bar{M}$ and U are onsite terms. Thus their competition can directly affect the band order in the valleys. To clarify this, in Fig. S7(d) we plot the schematic of the energy levels in the two valleys from the Hamiltonian H, without and with SOC. The tunability in our manuscript mainly focuses on the band inversion between the two conduction bands in the K' valley. Such band inversion gives rise to the change of the winding number and band topology as we discussed in the main text. From Fig. S7(d), it is clear the band order of the two conduction bands ($\lambda_{SO} + M_B - U$ and $\lambda_{SO} - M_A + U$) is determined by the

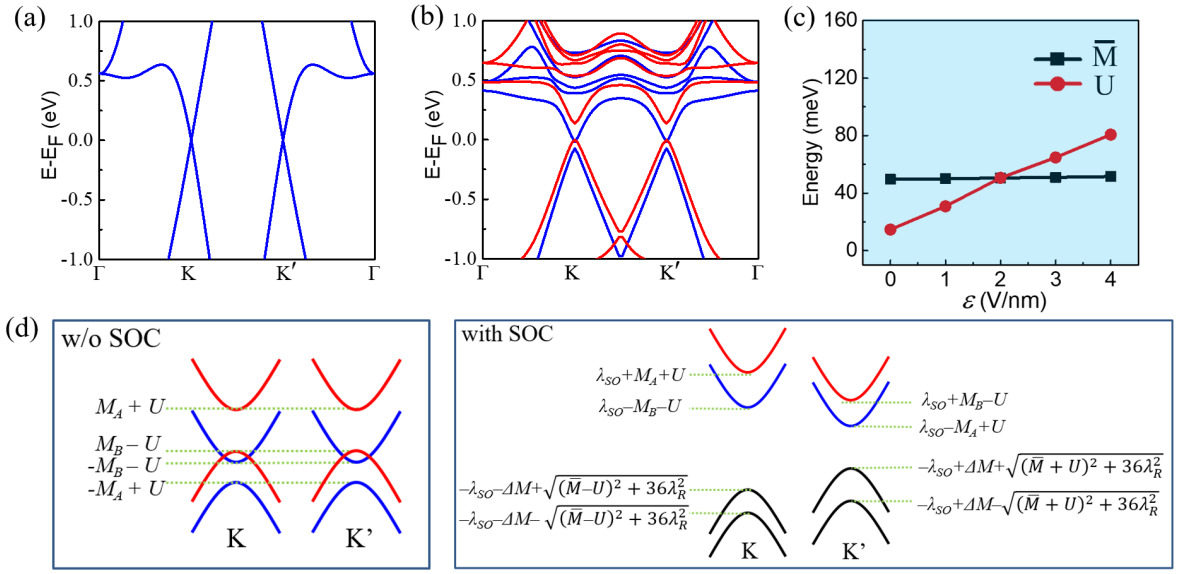

Fig. S 7: (a) and (b) Calculated electronic structure for pristine ML SbH and W-2×2 SbH without SOC. (c) $\mathcal{E}$-dependent $\bar{M}$ and U from DFT calculations. (d) Schematic of the energy levels of the bands in the two valleys without and with SOC, respectively. Here we assume $M_B < M_A < \lambda_{SO}$ and $M_A + M_B > 2U$, which is in agreement with the DFT calculations for ML W-2×2 SbH in Fig. 4(b). The red/blue curves in (b) and (d) indicate the spin-up/spin-down states.

competition between $\bar{M}$ and U. Note, the presence of SOC here alters the band gap in our system, but does not affect the conduction band ordering. Initially, $\bar{M}$ is larger than U in W-doped 2×2 SbH supercells (W-2×2 SbH), where $\bar{M}$ and U are obtained as around 51 meV and 14 meV, respectively, by fitting the effective model used in Fig. S7(d) with the DFT results from Fig. S7(b) and Fig. 4(b). To change the band order of the two conduction bands, we need $U > \bar{M}$. Considering previous demonstrations that U can be directly controlled by an electric field [29, 30], we propose to use an electric field to increase U and change the band order, as shown in Fig. 4.

When the perpendicular electric field is applied (from W to H), an additional staggered potential can be induced in the system, thus enhancing the total staggered potential. By fitting the model Hamiltonian to the DFT results, the electric field-dependent $\bar{M}$ and U are plotted in Fig. S7(c). One can see U is increased almost linearly by $\mathcal{E}$ and when $\mathcal{E} > 2$ V/nm, U is larger than $\bar{M}$, giving rise to the band inversion of the two conduction bands in Fig. 4. As we show in the main text, such band inversion can change the band topology and helicity of the optical response.

XI. EFFECTS OF CONCENTRATION AND DISORDER OF W ATOMS

In this section, we discuss the influence of the concentration and disorder of W atoms. The two key factors in our proposal are the exchange field, $\bar{M}$, and staggered potential, U, which are both induced by W atoms. Thus, it is expected that the W-concentration plays a significant role. To explore the influence of the W-concentration, we have performed electronic structure calculations for larger 4×4 SbH supercells doped with 1 to 8 W atoms, giving the W-concentration from 1/16 to 8/16, as shown in Figs. S8(a)-(h). The pattern of the W atoms for each concentration is set randomly. When the concentration is fixed, the electronic structure is robust against different W patterns, which will be illustrated in the following part about the effects of disorder.

The calculated electronic structure for different W-concentrations is shown in Figs. S8(i)-(p). We can clearly see that around the Fermi level, E_F, the electronic structure remains similar, but the spin splitting and the band gap are enhanced and reduced for larger W-concentrations, respectively. By fitting the electronic structure from the effective model [Fig. S7(d)] with the DFT results from Figs. S8(i)-(p), $\bar{M}$, U_i, and the band gap for different W-concentrations are plotted in Fig. S9(a). Remarkably, both $\bar{M}$ and U_i increase linearly with the W-concentration. Thus, the required external staggered potential to reverse the conduction band ordering, U_e, also has a linear dependence in the W-concentration, because of $U_C = U_i + U_e = \bar{M}$. As the W-concentration increases, the band gap decreases linearly as shown in Fig. S9(a). Notably, when the concentration is larger than 7/16, the valence bands and conduction bands cross. A novel gap can be opened at the band crossing points by Rashba SOC, giving a quantum anomalous Hall effect [5, 6]. However, the proposed optical response may not survive in such crossed bands. Thus, the W-concentration

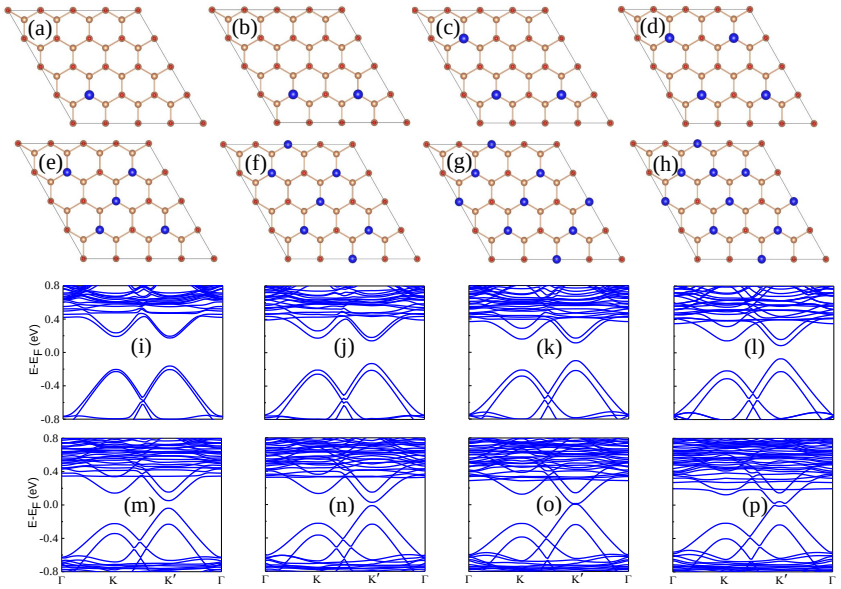

Fig. S 8: (a)-(h) The atomic structure of the 4×4 SbH supercell doped with 1 to 8 W atoms. (i)-(p) Calculated electronic structure for (a)-(h), respectively.

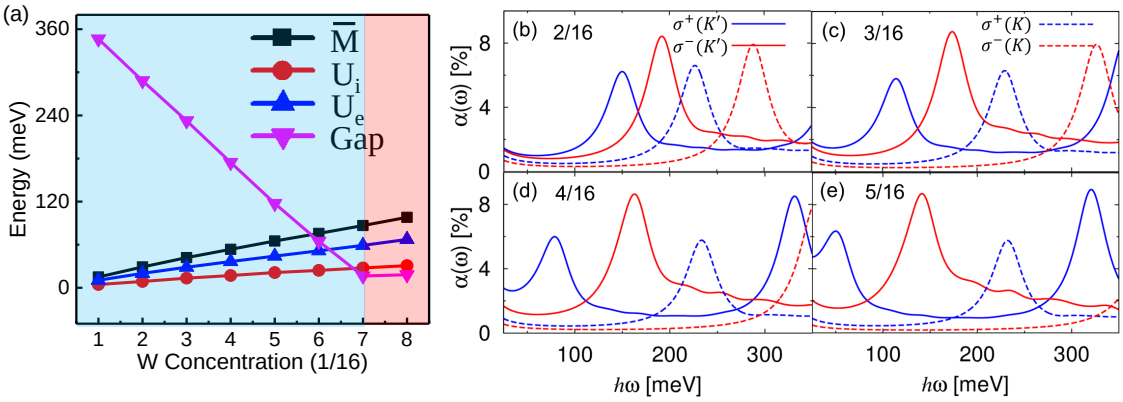

Fig. S 9: (a) The W-concentration dependent exchange field $\bar{M}$, intrinsic staggered potential U_i, required external staggered potential to reverse the conduction band ordering U_e (total critical staggered potential $U_c = U_i + U_e = \bar{M}$) and the band gap obtained from the electronic structure in Fig. S8, calculated using DFT. Absorption spectra for different W-concentrations: from (b) 2/16 to (e) 5/16.

range supporting our proposal is from 1/16 to 6/16. Such a large concentration range provides a suitable parameter space for the experimental realization of our proposal.

To further study the influence of the W-concentration on the optical properties, we calculate the absorption spectra for different W-concentrations in Figs. S9(b)-(e) by extracting relevant parameters from the corresponding electronic structure in Figs. S8(j)-(m). While there is a gradual decrease in the frequency of the first absorption peak, the qualitative features of the absorption spectra are preserved when the W-concentration is increased. Such a reduction in frequency is mainly due to the decrease of band gaps (shown in Fig. S8). These results corroborate that our main findings can be observed in a large concentration range and are therefore encouraging that an optical detection of the tunable band topology is experimentally feasible.

To understand the influence of the disorder of the doped W atoms, we have performed electronic structure calculations based on a 4×4 SbH supercell with special quasirandom structures [31]. Such an approach has been widely used in exploring the disorder effects based on a finite-size supercell [32]. With the W-concentration fixed as 4/16 or 25%, the same as in Fig. 4(a), we randomly create different atomic patterns for the 4 W atoms in the 4×4 SbH supercells,

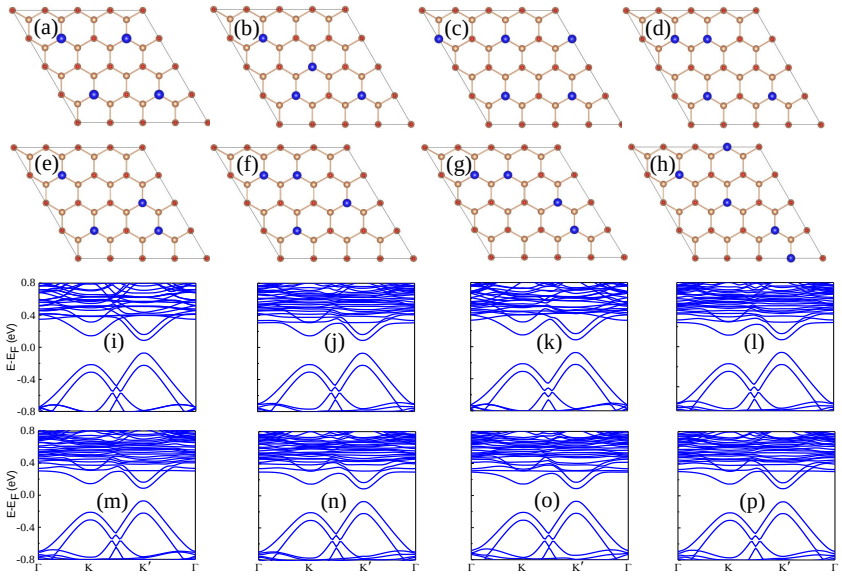

Fig. S 10: (a)-(h) Different atomic patterns for the 4×4 SbH supercell doped with 4 W atoms. (i)-(p) Calculated electronic structure for (a)-(h), respectively.

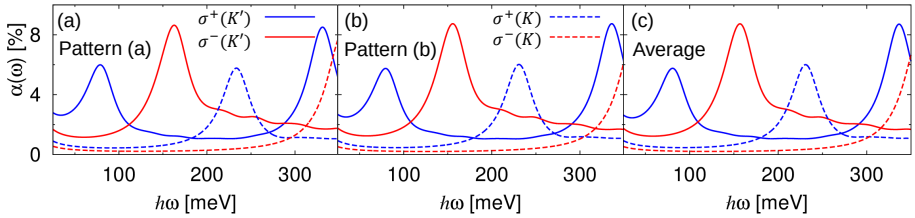

Fig. S 11: (a) and (b) Absorption spectra for different doping patterns (a) and (b) from Fig. S10 and (c) the average of all eight patterns in Fig. S10.

where only eight patterns are shown in Figs. S10(a)-(h).

For each of these atomic patterns in Figs. S10(a)-(h), the corresponding electronic structure is plotted in Figs. S10(i)-(p). Since the calculations show no obvious differences in their bands [Fig. S10(i)-(p)] at the two valleys near E_F, the disorder of W atoms does not significantly affect the low-energy properties. This can be understood from the observation that the desired gapped Dirac bands are related to Sb-p_x and p_y orbitals, while the bands from the W atoms, bonding with p_z orbitals, are far away from E_F in the two valleys, as shown in Fig. S4(b). The role of W atoms here primarily provides the exchange field and staggered potential to magnetize the Dirac bands around E_F. Since the exchange field and staggered potential are primarily determined by the concentration, rather than the distribution of the W atoms, the disorder of W atoms does not affect significantly our results.

We further illustrate in Fig. S11 the effect of disorder by showing the corresponding absorption spectra for different doping patterns (a) and (b), as well as an average of all the patterns in Fig. S10. We see that different patterns only have a minor influence on the absorption spectra. Therefore, our results are robust against the disorder of W atoms.

XII. EFFECTS OF STRAIN

Strain is very important for 2D materials as a versatile tool to engineer transport, optical, and topological properties. To explore the influence of strain in ML W-SbH, we employ a common in-plane biaxial strain to ML W-2×2 SbH, which corresponds to the relative change of the lattice constant by $\delta = (a - a_0)/a_0$, where a (a_0), is the strained (relaxed) lattice constant. Our DFT calculations show that the electronic structure of W-SbH can be strongly modified by the strain, as shown in Figs. S12(a) and (b). By fitting the effective model with the calculated bands, the strain-dependent

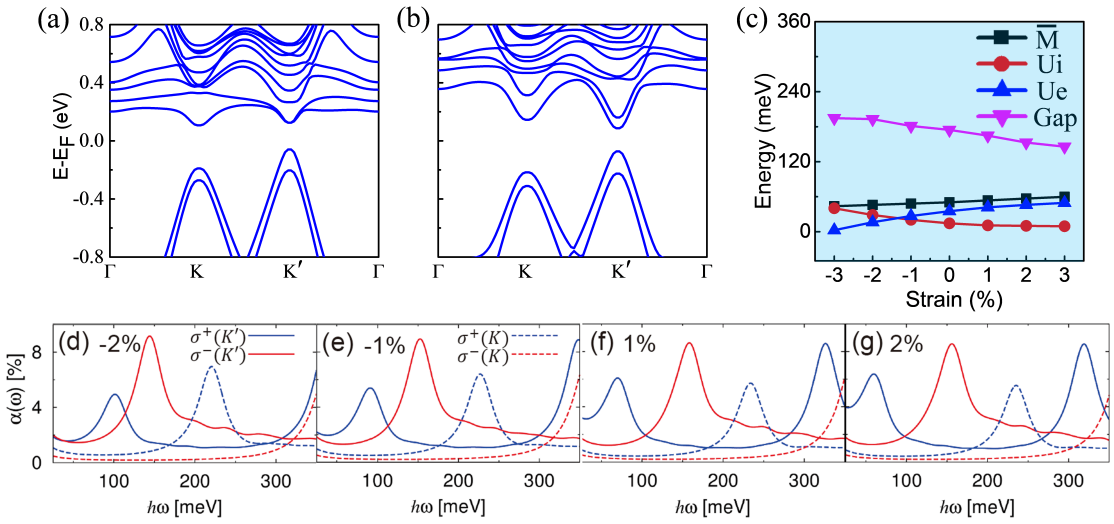

Fig. S 12: (a) and (b) Calculated electronic structure for the ML W-2×2 SbH under ∓3% in-plane strain, respectively. (c) The strain-dependent $\bar{M}$ and U obtained from DFT calculations. (d)-(g) Absorption spectra under in-plane strain from −2% to 2%.

$\bar{M}$ and U_i are plotted in Fig. S12(c). We can see U_i, can be enhanced when the lattice constant is decreased. By recalling $U_C = U_i + U_e = \bar{M}$, a suitable strain therefore makes the conduction band reversal possible at a smaller applied electric field.

To further explore the role of strain in the optical response, we have also calculated the absorption spectra for a series of strains shown in Figs. S12(d)-(g). The frequency of the first absorption peak decreases with larger strain, which is mainly due to the decreasing band gaps [see Fig. S12(c)], while the qualitative features remain unchanged. We note that experimentally our ML material forms a van der Waals heterostructure rather than chemical bonding with its substrate (h-BN), for which strain is minor. Therefore, our prediction of helicity reversal remains robust when strain is taken into account. The presence of strain can be used to tune the frequency of the first observed absorption peak.

[1] S. Zhang, S. Guo, Z. Chen, Y. Wang, H. Gao, J. Gómez-Herrero, P. Ares, F. Zamora, Z. Zhu, and H. Zeng, Recent Progress in 2D Group-VA Semiconductors: From Theory to Experiment, Chem. Soc. Rev. **47**, 982 (2018).

[2] R. Gui, H. Jin, Y. Sun, X. Jiang, and Z. Sun, Two-Dimensional Group-VA Nanomaterials Beyond Black Phosphorus: Synthetic Methods, Properties, Functional Nanostructures and Applications, J. Mater. Chem. A **7**, 25712 (2019).

[3] F. Reis, G. Li, L. Dudy, M. Bauernfeind, S. Glass, W. Hanke, R. Thomale, J. Schäfer, and R. Claessen, Bismuthene on a SiC substrate: A Candidate for a High-Temperature Quantum Spin Hall Material, Science **357**, 287 (2017).

[4] X. Zhang, W.-Y. Shan, and D. Xiao, Optical Selection Rule of Excitons in Gapped Chiral Fermion Systems, Phys. Rev. Lett. **120**, 077401 (2018).

[5] T. Zhou, J. Zhang, Y. Xue, B. Zhao, H. Zhang, H. Jiang, and Z. Yang, Quantum Spin-Quantum Anomalous Hall Effect with Tunable Edge States in Sb Monolayer-Based Heterostructures, Phys. Rev. B **94**, 235449 (2016).

[6] T. Zhou, J. Zhang, B. Zhao, H. Zhang, and Z. Yang, Quantum Spin-Quantum Anomalous Hall Insulators and Topological Transitions in Functionalized Sb(111) Monolayers, Nano Lett. **15**, 5149 (2015).

[7] Z. Song, C.-C. Liu, J. Yang, J. Han, M. Ye, B. Fu, Y. Yang, Q. Niu, J. Lu, and Y. Yao, Quantum Spin Hall Insulators and Quantum Valley Hall Insulators of BiX/SbX (X=H, F, Cl and Br) Monolayers with a Record Bulk Band Gap, NPG Asia Mater. **6**, e147 (2014).

[8] A. J. Mannix, B. Kiraly, M. C. Hersam, and N. P. Guisinger, Synthesis and Chemistry of Elemental 2D Materials, Nat. Rev. Chem. **1**, 0014 (2017).

[9] S. R. Schofield, P. Studer, C. F. Hirjibehedin, N. J. Curson, G. Aeppli, and D. R. Bowler, Quantum Engineering at the Silicon Surface using Dangling Bonds, Nat. Commun. **4**, 1649 (2013).

[10] C. Kittel, *Introduction to Solid State Physics*, 5th ed. (Wiley, New York, 1976).

[11] M. Pumera and C. H. A. Wong, Graphane and Hydrogenated Graphene, Chem. Soc. Rev. **42**, 5987 (2013).

[12] F. Karlický, K. K. R. Datta, M. Otyepka, and R. Zbořil, Halogenated Graphenes: Rapidly Growing Family of Graphene Derivatives, ACS Nano **7**, 6434 (2013).

[13] M. Rohlfing, and S. G. Louie, Electron-Hole Excitations and Optical Spectra from First Principles, Phys. Rev. B **62**, 4927 (2000).

[14] B. Scharf, T. Frank, M. Gmitra, J. Fabian, I. Žutić, and V. Perebeinos, Excitonic Stark Effect in MoS_2 Monolayers, Phys. Rev. B **94**, 245434 (2016).

[15] B. Scharf, G. Xu, A. Matos-Abiague, and I. Žutić, Magnetic Proximity Effects in Transition-Metal Dichalcogenides: Converting Excitons, Phys. Rev. Lett. **119**, 127403 (2017).

[16] If the non-interacting single-particle/quasiparticle states are spin-degenerate, the exciton states can be categorized as singlet and triplet states, whose BSE (III.1) is calculated only from the real-space single-particle/quasiparticle wave functions and contains the kernels $\mathcal{K} = \mathcal{K}^{\rm d} + 2\mathcal{K}^{\rm x}$ and $\mathcal{K} = \mathcal{K}^{\rm d}$, respectively.

[17] C. Zhang, H. Wang, W. Chan, C. Manolatou, and F. Rana, Absorption of Light by Excitons and Trions in Monolayers of Metal Dichalcogenide MoS_2: Experiments and Theory, Phys. Rev. B **89**, 205436 (2014).

[18] D. Van Tuan, B. Scharf, Z. Wang, J. Shan, K. F. Mak, I. Žutić, and H. Dery, Probing Many-Body Interactions in Monolayer Transition-Metal Dichalcogenides, Phys. Rev. B **99**, 085301 (2019).

[19] L. V. Keldysh, Coulomb Interaction in Thin Semiconductor and Semimetal Films, JETP Lett. **29**, 658 (1979).

[20] P. Cudazzo, I. V. Tokatly, and A. Rubio, Dielectric Screening in Two-Dimensional Insulators: Implications for Excitonic and Impurity States in Graphane, Phys. Rev. B **84**, 085406 (2011).

[21] T. C. Berkelbach, M. S. Hybertsen, and D. R. Reichman, Theory of Neutral and Charged Excitons in Monolayer Transition Metal Dichalcogenides, Phys. Rev. B **88**, 045318 (2013); Bright and Dark Singlet Excitons via Linear and Two-Photon Spectroscopy in Monolayer Transition-Metal Dichalcogenides, *ibid.* **92**, 085413 (2015).

[22] T. Cao, M. Wu, and S. G. Louie, Unifying Optical Selection Rules for Excitons in Two Dimensions: Band Topology and Winding Numbers, Phys. Rev. Lett. **120**, 087402 (2018).

[23] D. J. Singh and L. Nordstrom, *Planewaves, Pseudopotentials, and the LAPW Method*, 2nd ed. (Springer, New York, 2006).

[24] P. Blaha, K. Schwarz, G. Madsen, D. Kvasnicka, and J. Luitz, WIEN2k, An Augmented Plane Wave + Local Orbitals Program for Calculating Crystal Properties, Techn. Universtät, Wien, Austria, 2001.

[25] J. P. Perdew, K. Burke, and M. Ernzerhof, Generalized Gradient Approximation Made Simple, Phys. Rev. Lett. **77**, 3865 (1996).

[26] Y. Yao, L. Kleinman, A. H. MacDonald, J. Sinova, T. Jungwirth, D.-S. Wang, E. Wang, and Q. Niu, First Principles Calculation of Anomalous Hall Conductivity in Ferromagnetic bcc Fe, Phys. Rev. Lett. **92**, 037204 (2004).

[27] K. F. Mak, K. L. McGill, J. Park and P. L. McEuen, The valley Hall effect in MoS_2 Transistors, Science **344**, 1489 (2014).

[28] T. Zhou, J. Zhang, H. Jiang, I. Žutić, and Z. Yang, Giant Spin-Valley Polarization and Multiple Hall Effects in Functionalized Bismuth Monolayers, npj Quant. Mater. **3**, 39 (2018).

[29] I. Martin, Y. M. Blanter, and A. F. Morpurgo, Topological Confinement in Bilayer Graphene, Phys. Rev. Lett. **10**, 036804 (2008).

[30] J. Li, R-X Zhang, Z. Yin, J. Zhang, K. Watanabe, T. Taniguchi, C. Liu, and J. Zhu, A Valley Valve and Electron Beam Splitter, Science **362**, 1149 (2018).

[31] A. Zunger, S.-H. Wei, L. G. Ferreira, and J. E. Bernard, Special Quasirandom Structures, Phys. Rev. Lett. **65**, 353 (1990).

[32] V. Saltas, D. Horlait, E. N. Sgourou, F. Vallianatos, and A. Chroneos, Modelling Solid Solutions with Cluster Expansion, Special Quasirandom Structures, and Thermodynamic Approaches, Appl. Phys. Rev. **4**, 041301 (2017).